

## COSMIC-RAY ANTIPROTON FLUX IN THE ENERGY RANGE FROM 200 TO 600 MeV

A. MOISEEV,<sup>1,2</sup> K. YOSHIMURA,<sup>3</sup> I. UEDA,<sup>3</sup> K. ANRAKU,<sup>4</sup> R. GOLDEN,<sup>5,6</sup> M. IMORI,<sup>3</sup> S. INABA,<sup>4</sup>  
B. KIMBELL,<sup>5</sup> N. KIMURA,<sup>4</sup> Y. MAKIDA,<sup>4</sup> H. MATSUMOTO,<sup>7</sup> H. MATSUNAGA,<sup>3</sup> J. MITCHELL,<sup>1</sup>  
M. MOTOKI,<sup>7</sup> J. NISHIMURA,<sup>8</sup> M. NOZAKI,<sup>7</sup> S. ORITO,<sup>3</sup> J. ORMES,<sup>1</sup> T. SAEKI,<sup>3</sup> E. S. SEO,<sup>9</sup>  
S. STOCHAJ,<sup>5</sup> R. STREITMATTER,<sup>1</sup> J. SUZUKI,<sup>4</sup> K. TANAKA,<sup>4</sup> N. YAJIMA,<sup>8</sup> T. YAMAGAMI,<sup>8</sup>  
A. YAMAMOTO,<sup>4</sup> AND T. YOSHIDA<sup>3</sup>  
(BESS COLLABORATION)

Received 1996 May 22; accepted 1996 July 24

### ABSTRACT

We have studied the low-energy antiprotons in the cosmic rays by utilizing data obtained by the Balloon-borne Experiment with a Superconducting magnetic rigidity Spectrometer (BESS) flown in 1993 July from Lynn Lake, Manitoba, Canada. A detailed description of the event selection criteria and background corrections is given. Seven antiprotons are found that give an antiproton flux of  $6.4^{+5.5}_{-3.5} \times 10^{-3} (\text{m}^2 \text{ sr s GeV})^{-1}$  and an antiproton/proton ratio of  $5.2^{+4.4}_{-2.8} \times 10^{-6}$  in the 200–600 MeV energy range. These results are consistent with a secondary origin of low-energy cosmic-ray antiprotons within our uncertainties, but they still require the precise measurement of the spectrum shape below 500 MeV to clarify exactly the model of particle propagation and possible contributions from exotic sources.

*Subject headings:* balloons — cosmic rays — elementary particles

### 1. INTRODUCTION

The first reports of the detection of cosmic-ray antiprotons ( $\bar{p}$ 's) were published in 1979 (Golden et al. 1979; Bogomolov et al. 1979). Shortly after these measurements, Buffington, Schindler, & Pennypacker 1981 measured an unexpectedly large  $\bar{p}$  flux in the few hundred MeV kinetic energy range. Subsequent measurements made at these low energies (PBAR: Ahlen et al. 1988 and Salamon et al. 1990; LEAP: Streitmatter et al. 1989 and Stochaj et al. 1990) failed to verify this claim. Both of these follow-up experiments were design to detect antiprotons fluxes near the level measured by Buffington et al. The observed fluxes were more than a decade below the Buffington et al. level and were at or below the lower limit of sensitivity for these instruments. Hence, these results were reported as upper limits (Fig. 1). A new generation of experiments, designed with greater sensitivity (Yoshimura et al. 1995; Mitchell et al. 1996), are beginning to make more precise measurements at the low-energy range. These observations will help us understand whether the antiproton components of the cosmic rays can be understood within the framework of the standard model of cosmic-ray propagation or whether more exotic models of antiproton production are required (see Gaisser 1990). Here we provide extended details and interpretation of the results (Yoshimura et al. 1995) of the first flight of the Balloon-borne Experiment with a Superconducting magnet rigidity Spectrometer (BESS).

The motivation of the BESS experiment was to perform observations that will further the understanding of the origin of antiprotons in the galactic cosmic rays. Some cosmic-ray antiprotons are secondary in nature, being produced in the collisions of primary cosmic-ray nuclei with the interstellar medium. These  $\bar{p}$ 's are stored, without further interactions or annihilations, in the interstellar magnetic fields just like their progenitors. The expected  $\bar{p}$  energy spectrum and the antiproton/proton ratio ( $\bar{p}/p$ ) have been calculated by several authors (see Stephens & Golden 1987 and references therein, also Webber & Potgieter 1989) for various cosmic-ray propagation models. Simon & Heinbach (1996) calculated the interstellar antiproton flux in the diffusive reacceleration model. Gaisser & Shaeffer (1992) calculated the extrema for the  $\bar{p}/p$ . These ratios have been modulated for conditions of solar maximum and minimum, and they are shown in Figure 1 along with the available low-energy range experimental results. Throughout this paper, the solar modulation effects are calculated according to Gleeson & Axford (1968).

Some of the early experimental results reported an excess of  $\bar{p}$ 's over the number expected by secondary production calculations. This excess suggested either an instrumental problem or a source of “primary” antimatter. Gamma-ray observations placed a strict limit on the antimatter content of our Galaxy and in the local clusters of galaxies out to 10 Mpc. Hence, antiprotons could not be a primary component of the cosmic rays accelerated in our Galaxy (Steigman 1976). Several different theories were advanced to explain the excess of antiprotons. These included exotic processes such as the evaporation of primordial black holes (e.g., see Kiraly, Wdowczyk, & Wolfendale 1981; Turner 1982; Maki, Mitsui, & Orito 1996) or the annihilation of supersymmetrical particles gravitationally bound to the Galaxy (e.g., see Silk & Srednicki 1984; Rudaz & Stecker 1988; Jungman & Kamionkowski 1994; Bottino et al. 1995).

Over most energy ranges, the number of secondary antiprotons dominate the number of  $\bar{p}$ 's produced by any of the exotic models. However, the phase space for a collisionally

<sup>1</sup> National Aeronautics and Space Administration, Goddard Space Flight Center (NASA/GSFC), Greenbelt, MD 20771.

<sup>2</sup> NAS/NRC Resident Research Associate, on leave from the Moscow Engineering Physics Institute, Moscow, Russia.

<sup>3</sup> University of Tokyo, Bunkyo-ku, Tokyo 113, Japan.

<sup>4</sup> National Laboratory for High Energy Physics (KEK), Tsukuba, Ibaraki, Japan.

<sup>5</sup> New Mexico State University, Las Cruces, NM 88003.

<sup>6</sup> Deceased.

<sup>7</sup> Kobe University, Kobe, Hyogo, Japan.

<sup>8</sup> The Institute of Space and Astronautical Science (ISAS), 3-3-3, Yoshinodai, Sagamihara-shi, Kanagawa 229, Japan.

<sup>9</sup> University of Maryland, College Park, MD 20742.

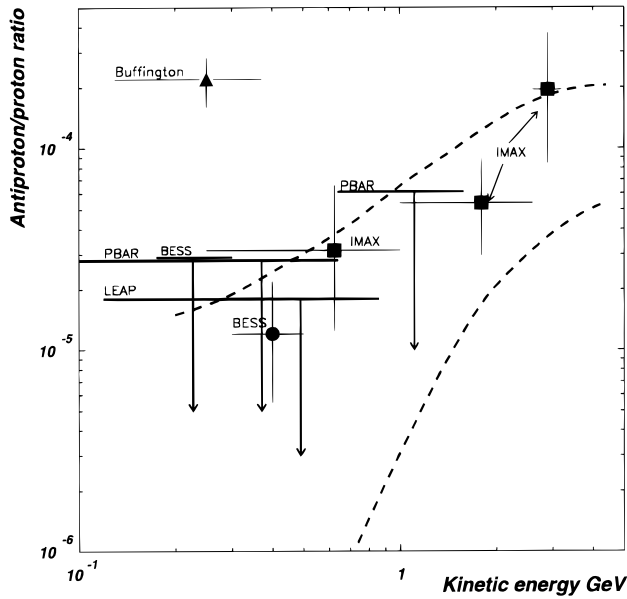


FIG. 1.—Current results in the low-energy antiproton/proton ratio measurements: *filled triangle*: Buffington et al. (1981); *filled squares*: IMAX (Mitchell et al. 1996); *filled circle*: BESS-93 (Yoshimura et al. 1995); upper limits: LEAP (Stochaj et al. 1990); PBAR (Salamon et al. 1990); BESS (Yoshimura et al. 1995). *Dashed lines*: maximum and minimum, calculated by Gaisser & Shaeffer (1992) according to Leaky Box model and modulated for conditions of solar maximum and minimum.

produced  $\bar{p}$  below 1 GeV decreases extremely rapidly. This leaves the region below 1 GeV as a potential “window” in which antiprotons from these exotic sources could be detected against the “background” of collisionally produced  $\bar{p}$ 's.

The first flight of the BESS instrument was from Lynn Lake, Manitoba, Canada, on 1993 July 26. The main goal of this flight was to unambiguously identify antiprotons and measure the  $\bar{p}$  flux in the energy range from 200 to 600 MeV. The initial results of this flight, based on the observation of four antiprotons in the energy range 300-500 MeV, were reported in Yoshimura et al. (1995).

In this paper we explore, in detail, an alternate analysis of the antiproton data. Using this new approach, we have been able to extend the range of the  $\bar{p}$  measurement up to 600 MeV. The sensitivity of this approach with respect to the selection criteria is examined. Various possible sources of background are considered as well. The experimental

details set forth in this paper will provide a template with which the data from subsequent flights of this payload will be analyzed.

## 2. BESS: BASIC STRUCTURE AND PRINCIPLE OF OPERATION

The basic BESS instrument is a superconducting magnetic spectrometer that is used to determine the rigidity and charge sign of high-energy-charged particles (Yamamoto et al. 1994). The basic requirement of such an instrument is to provide statistically significant results during the limited-duration balloon experiment. Given the expected secondary flux, the experiment requires a geometrical factor close to 1 m<sup>2</sup> sr.

Particles are identified by measuring their mass. The relationship  $m^2 = R^2 Z^2 (1/\beta^2 - 1)$  can easily be derived from the relativistic relationships and the definition of rigidity as momentum per unit charge. BESS measures the particle rigidity,  $R$ , by reconstructing the particle track in the instrument's magnetic field by means of drift chambers. The particle velocity  $\beta$  is determined by a time-of-flight (TOF) measurement. The knowledge of particle charge,  $Z$ , comes from ionization-loss measurements ( $\sim Z^2$ ) made in the TOF scintillators. The ionization-loss measurements are also helpful in identifying light subrelativistic particles. The particle charge sign is determined from the direction of the trajectory and its deflection.

To realize this large area solid angle product, a cylindrical geometry was chosen. Its collecting power is a factor of 10–30 times that of previously flown balloon-borne magnetic spectrometers (MASS: Golden et al. 1991; IMAX: Mitchell et al. 1993; HEAT: Tomash et al. 1995), but it obviously is more complicated. The basic structure of the BESS spectrometer is shown in Figure 2. It consists of the following detectors: the main drift chamber (JET), inner drift chamber (IDC), the outer drift chamber (ODC), paddle scintillation counters for triggering and TOF measurement, and the superconducting solenoid. All of these detectors, as well as microcomputers and other electronics, are enclosed in an aluminum cylindrical hermetic-pressurized vessel 1.5 m diameter and 3.2 m in length. Its 2 mm thick walls contain the pressure to maintain normal atmospheric conditions for the instrument during flight. The batteries are situated outside the vessel. The total weight is about 2100 kg, and the power consumption is about 1200 W. This con-

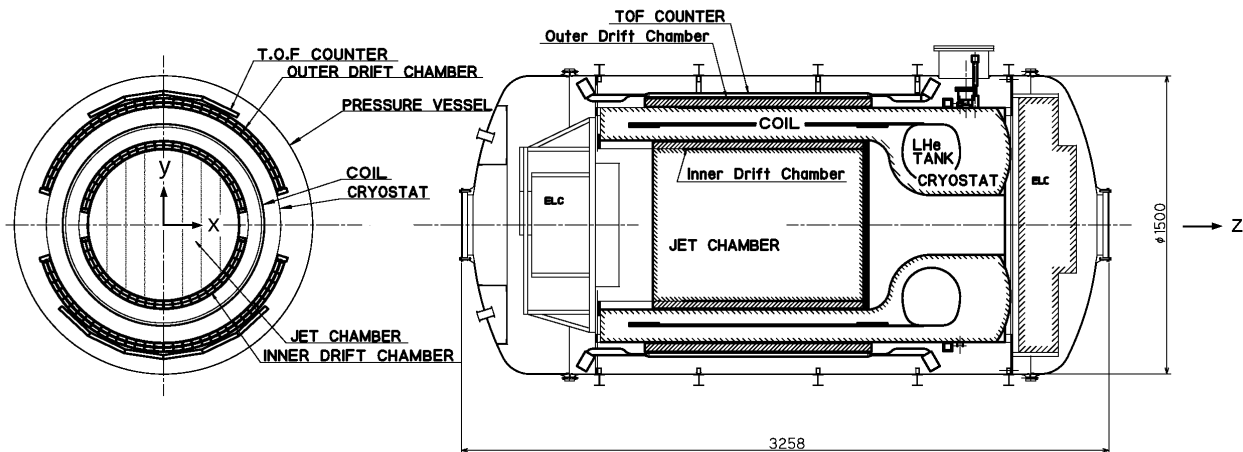


FIG. 2.—Basic structure of BESS

figuration provides an instrument geometrical factor  $G = 0.4 \pm 0.03 \text{ m}^2 \text{ sr}$ . At low energy,  $G$  decreases slightly, and this effect ( $\sim 5\%$ ) is included in its uncertainty.

### 2.1. Detectors and Parts

#### 2.1.1. Superconducting Solenoidal Magnet

The superconducting solenoidal magnet is the central core component of the rigidity spectrometer (Yamamoto et al. 1988; Makida et al. 1992). It consists of a 1 m diameter and 1 m long, 3368 turn solenoidal coil made from four layers of 1.2 mm thick NbTi/Cu/Al wire laid on the inner surface of the aluminum support cylinder and installed inside a double-shielded thermal cryostat. The coil is indirectly cooled by liquid helium from a Dewar with 150 liters capacity, sufficient to keep the magnet cold for 6 days. A magnetic field of about 1 T is generated inside the 0.8 m diameter and 1 m long solenoid when the magnet is charged with 430 A. The field uniformity is about 15%. The total weight of magnet with helium is 430 kg.

#### 2.1.2. JET Chamber

The JET chamber<sup>10</sup> is a cylindrical drift chamber with a total tracking volume of 0.754 m in diameter by 1 m in length. It is located in the bore of the magnet solenoid and provides the high-resolution particle tracking through the magnetic field; in combination with the magnetic field, it forms the rigidity spectrometer. The chamber volume is divided into four sections by vertical cathode planes formed by one hundred 200  $\mu\text{m}$  diameter aluminum wires mounted with 6.7 mm pitch. The sense wire plane bisecting each section is made up of 20  $\mu\text{m}$  gold-plated tungsten-rhenium sense wires and 200  $\mu\text{m}$  gold-plated aluminum potential wires laid out alternatively with 6.7 mm pitch. The sense wires are slightly alternatively shifted ( $\delta x = \pm 0.5 \text{ mm}$ ) with respect to the potential wire plane in order to resolve the right-left ambiguity inherent in the drift chamber technique. The coordinate of the track is determined by measuring the time it takes for the electrons, produced by the passage of the energetic ionizing charged particle, to drift from the particle track to the closest sense wire. This time is determined by the distance between the sense wire and the track. Since we know precisely the map of sense wires positions, we can determine on which side of the potential wire plane the particle passed. The gas mixture 90%  $\text{CO}_2 + 10\% \text{ Ar}$  was used because of its relatively low (about 7 mm  $\mu\text{s}^{-1}$ ) drift velocity, thus allowing drift times (and thereby the “ $x$ ” positions) to be measured with better precision. This mixture is also suitable for filling the entire gondola interior, eliminating the risk of gas leaks into or out of the JET chamber volume. The total weight of the JET chamber is 60 kg.

The positions of the particle track are measured in three dimensions. In the bending plane ( $x, y$ ), where the most precise measurement is required, a series of points (one from each sense wire) along the track in the bending direction is obtained by measuring the drift time. Along the  $z$ -axis of the chamber, the position is determined by measuring the charge collected on both ends of each resistive sense wire; the  $z$ -coordinate is determined from the ratio of signals at the two ends.

Operating with 28.5 MHz flash analog-to-digital converters, the amplified pulse from each sense wire is read out.

Each output contains information about charge, timing, and pulse shape. The high sampling frequency allows multiple “hits” to be identified and separately analyzed. There are 24 measurements in the  $x$ - $y$  plane and 16 (in two central cells) or 8 (in two outer cells) measurements along the chamber axis  $z$ . This information allows complicated events with interactions as well as multiple-track events to be reconstructed.

The average spatial resolution in the bending plane is about 200  $\mu\text{m}$ . The resolution along the chamber is about 2.5 cm. The momentum resolution at 1 GV is 0.5%, corresponding to a maximum detectable rigidity (MDR) of 200 GV.

#### 2.1.3. IDC and ODC

The cell-type double layer inner and outer drift chambers (called IDC and ODC, respectively) are located just inside (the IDC) and outside (the ODC) the magnet solenoid. The IDC (ODC) is 1.06 (1.18) m long and 36 (44) mm thick, situated on a mean radius 402 (616) mm. The design of both chambers is similar. Each chamber has two layers that are each 12 mm thick. The sense and field wires are alternately laid with 44.6–48.9 mm pitch (they differ for each cell and layer) in the center of each layer, creating 50 mm wide cells. The fast on-line estimation of the track coordinate, which has about 50 mm resolution, is taken from the position of the hit sense wire (or of the appropriate cell number). The cells of the IDCs and ODCs, by themselves, form a low-resolution rigidity-measuring device that is analyzed in real time to preferentially select negative curvature events while sampling the much higher abundance positive curvature events in a scheme to be described in detail below.

The average IDC and ODC resolution in the bending plane is also 200  $\mu\text{m}$ . The position along a chamber ( $z$ -coordinate) is determined by measuring the charge induced on vernier pads surrounding each sense wire. The resolution in this coordinate is estimated to be 350  $\mu\text{m}$ .

#### 2.1.4. Scintillation Paddle System

The signals from the scintillator paddles are used for three different purposes: fast (first-level) trigger, TOF measurement, and energy-deposit measurement. There are two sets of scintillation counters that are situated just on the outer surface of the ODC at a radius of 65 cm. The upper one is divided into four paddles, the lower one into six paddles, each  $110 \times 20 \times 2 \text{ cm}^3$ . The amplitudes of the light pulses are measured by photomultiplier tubes (PMTs) located at both ends of each paddle; they determine the position of the particle along the paddle length. Each paddle has a light-emitting diode (LED) for calibration. Because of the high magnetic field (about 1.8 kG at phototube locations) 19-stage Hamamatsu tubes H2611SXA, which are tolerant to operation in high magnetic fields, are used. They are mounted with their axes aligned within  $15^\circ$  of the local magnetic flux lines.

For creating a first-level trigger (T0), the pulses are taken from the 19th dynode of the paddle phototubes. There are two different thresholds for this trigger: the low one accepts the most charged particles, including minimum ionizing particles, and the higher one accepts all higher charges. For timing measurement, the T0 pulse is taken as “start,” and the signal from the phototube’s anode is taken as “stop.” The time resolution obtained from the flight data is about 300 ps. The pulse from the 18th dynode is analyzed to measure  $dE/dx$ .

<sup>10</sup> Named for its ability to see “jets” from interactions in colliding-beam experiments.

## 2.2. Triggering

Because of the high flux of protons, BESS has a complex triggering scheme (Fig. 3). The objective is to have high efficiency for antiprotons and antihelium while obtaining a clean, well-understood sample of proton and helium events. There are two levels of trigger. The "fast trigger," mentioned above, has three modes ("T0 low" for all charged particles, "T0 high" for heavier nuclei, especially helium, and "T0 gamma" to look for gamma-ray events). The "T0 gamma" trigger was sampled at 1/256 because of its high rate. This trigger is background dominated and will not be discussed here.

The "track trigger" (TT) creates a "selected" sample of events by doing two operations: cleaning the data sample by accepting only eight predefined types of events based on a number of hits in the drift chambers (hit-pattern selection) and, after that, preferentially selecting negative curvature events (rigidity selection). Both of these selections operate by using the ODC and IDC to make a rough estimate of the location and configuration of the track in the JET chamber. The most possible configurations of hit ODC (IDC) cell patterns are stored in 2 Mbyte ROM, and the on-board processing compares these eight patterns to each event. The hit-pattern selection removes most of the shower and empty JET events. The events that pass this selection undergo the rigidity selection. An on-line estimate of deflection is made using a look-up table based on the ODC and IDC cells that were hit. TT is generated only if this deflection is more negative than the preset (adjustable) threshold that is assigned to that particular hit pattern (stored in ROM). The TT selection is designed to accept as many clear events with negative curvatures as possible. This data set is recorded on board and contains the antiproton events. The curvature

thresholds of accepted deflections are adjusted to allow the highest acceptable trigger rate that will not exceed the available capacity of the data recorder (about 100 Hz).

The outputs from TT and from T0 are combined by "trigger logic." The resulting signal and T0 signal are put into countdown circuit (CD), creating a 12 bit master trigger signal. The CD allows a fraction of T0 triggers to bypass all other selections and to create a so-called "unbiased countdown" sample. The low-threshold output of T0 is sampled by CD at 1/140 (mostly protons), and the higher threshold at 1/40 (enriched by helium and heavier nuclei). This sample gives a direct measurement of the incident charged particle flux and serves to check the operation of the trigger system.

## 3. FLIGHT

BESS was successfully launched by a balloon from Lynn Lake, Manitoba, Canada, on 1993 July 26 (Anraku et al. 1994). The float altitude was 36.5 km, and the residual atmosphere was about  $5 \text{ g cm}^{-2}$ . The total flight duration was 17 hr, the scientific data were taken for 13 hr, and the total data acquisition time was 11.77 hr. After correction for an instrument dead time, the total live time  $T_{\text{live}}$  was 8.61 hr.

During the flight, 3.6 million events were recorded. After termination, the instrument was recovered successfully without damage. The latitude varied from  $56^{\circ}48'$  north to  $57^{\circ}52'$  north, and longitude from  $101^{\circ}25'$  west to  $117^{\circ}30'$  west; the corresponding geomagnetic cutoff was 0.34–0.43 GV.

## 4. FLIGHT DATA ANALYSIS

### 4.1. Rigidity Measurement

The particle curvature,  $R^{-1}$ , is determined directly by the drift chambers using the coordinate information from JET and IDC chambers and a circular fitting routine. These drift chambers are sampled continuously, and the data set may contain multiple hits from one or more track(s) in the chambers. Only hits having appropriate amplitude of signal participate in the track reconstruction. To find hits associated with a track, a track is assumed, and all hits within 1 mm ( $\leq 5 \sigma$ ) are included in the reconstruction. The fitting is repeated several times, adding or discarding points depending on their position relative to the fitted track. The resulting value of rigidity,  $R$ , is corrected for the nonuniformity of the magnetic field. This procedure gives an accuracy for the rigidity determination as  $\Delta R/R = 0.005 \text{ GV}^{-1} R$ .<sup>11</sup> Finally, the rigidity is corrected for the angle of the track in the orthogonal to the bending plane ( $y, z$ ). The fitted trajectory determines the path length; dividing path length by measured TOF determines the particle velocity.

### 4.2. Event Selections

To reduce the data set to a manageable size, a data summary tape (DST) is prepared for scientific analysis. It contains all necessary information for each event: triggering information, TOF data (timing and charges for each counter), JET data (numbers and qualitative characteristics of hits, parameters of fitted track), IDC and ODC data, and combined track data (fitted rigidity, curvature characteristics,  $\chi^2$  values for the curvature fits,  $dE/dx$  for each detector,  $\int dlB$  along track, path length, and reconstructed

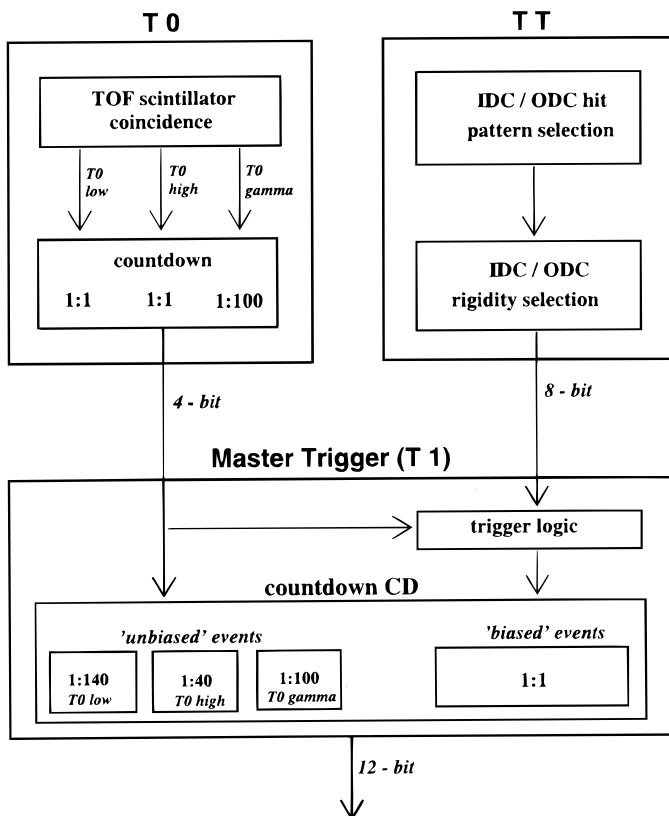


FIG. 3.—Triggering logic

<sup>11</sup> The curvature uncertainty distribution has a non-Gaussian tail important for high energy spectral measurements (Seo et al. 1996) but not important for this analysis.

particle mass). The DST contains 3,635,139 events in total, including 517,148 T0 low CD events. To find the events that have clear, reliable, and easily recognizable characteristics, the following selections are applied during ground-based analysis:

1. Events should have one track in the JET chamber and one hit in each TOF counter.
2. At least one hit in each of the upper two and lower two layers of IDCs must have been used in the track fitting.
3. The number of JET hits used for fitting in the bending plane should be  $\geq 11$ , and in the orthogonal plane  $\geq 5$ .
4. There should be  $\leq 20$  extra hits in the JET chamber not associated with the fitted track.
5. In a plane of bending, the  $\chi^2_{\text{reduced}}$  of the fit should be less than 4, and in the orthogonal plane along the chamber, it should be less than 3.5.
6. The reconstructed track should pass less than 500 mm in the  $z$ -direction from the center of TOF paddles.
7. The position along the chamber ( $z$ -coordinate) determined by the left-right time difference from TOF counters should be not more than 80 mm from the same coordinate of the reconstructed track position.
8. The ratio of the pulse heights from the left and right PMTs should be consistent with the  $z$ -coordinate of the reconstructed track.

These criteria are highly effective in removing multiple-particle events and those without a clear track in the JET chamber.

The hit-pattern selection criteria used on board the payload (described in § 2.2 above) were applied on the ground to the CD sample in order to assure that all analyzed events pass the same selections. The only difference between TT and CD samples after applying these cuts is connected with the “rigidity selection.” Let us recall that this selection was applied to the TT sample on board the payload in order to capture the negative curvature events. The effect of the rigidity selection will be described later.

In total, 1,580,030 events, including 72,144 events from the T0 low CD sample, passed through all the mentioned cuts, and they form the data set for further analysis.

#### 4.3. Proton and Antiproton Selection

The next step in the data analysis was to find the criteria to be applied to the data set in order to find clearly identified antiproton events well separated from other negative particles ( $e^-$ ,  $\mu^-$ ,  $\pi^-$ ). In order to assure confidence in the antiproton identification, selections used during the initial BESS-93 data analysis (Yoshimura et al. 1995) were rather strict. Now confident in this identification, we relax these selections in order to improve the statistics and extend the energy range up to 600 MeV.

The steps of our data analysis are as follows: first, all upward-moving particles are eliminated in order to prevent a proton from imitating an antiproton. The resolution of the TOF ( $\beta^{-1}$ ) measurement  $\sigma_{\text{TOF}} = 0.065$  was obtained from the flight data negative curvature events distribution (mostly relativistic) and agrees with estimates from the TOF timing resolution. If we compare upward- and downward-moving particles having  $1/\beta = 1$ , they will be separated by about  $30\sigma_{\text{TOF}}$ , which gives a strong confidence in the determination of the particle flight direction.

The next step involves selecting singly charged particles by using the pulse-height information from the TOF scintil-

lators (proportional to the particle ionization energy loss). We remove particles with  $Z \geq 2$  very easily by setting the rigidity-dependent upper limit for energy losses ( $dE/dx$ ) in the scintillator using the  $dE/dx$  versus curvature  $R^{-1}$  plot (Fig. 4). We also remove light particles at low rigidity by requiring  $dE/dx$  to exceed the minimum level for this value. This operation keeps about 95% of the detected protons and antiprotons while removing light and heavy particles. A search for antihelium is the subject of a separate study.

The application of these simple selections is sufficient for the clear identification of antiprotons as shown in Figure 5a, all events before  $dE/dx$  selection, and in Figure 5b, after this selection. We choose the variables  $(1/R^2, 1/\beta^2)$  because particles of a given mass all lie on a straight line of slope  $m^2/Z^2$  passing through the point (0, 1). We assign the negative sign for the square curvature of events having the negative sign of their trajectory curvature. We clearly see a wide proton line, some heavier residual nuclei, and positive light particles on the right side of the plot. We see a cloud of high rigidity,  $1/\beta = 1$  negative particles on the left side of the plot. Above this cloud, we see seven events marked by stars that form a straight line where the antiprotons are expected to lie. All of them lie well above the line labeled  $5\sigma$ . This line is  $5\sigma_{\text{TOF}}$  from the response for relativistic light particles ( $\pi^-$ ,  $\mu^-$ ,  $e^-$ ) and is used as our antiproton acceptance criterion. There are no background events that lie off the antiproton line. We can use these seven events to determine the value  $(0.95 \pm 0.06)$  GeV for their mass. It agrees very well with the antiproton mass.

Each of these seven events were checked in detail to look for anything unusual or ambiguous about the track. All candidates demonstrated perfect tracks.

The mismeasured curvature of a track with good  $\chi^2$  cannot be responsible for these events. The minimum curvature for our antiprotons is about  $330\sigma$  in rigidity from the corresponding velocity proton. To explore the probability that some kind of scattering (Coulomb or nuclear) could simulate the incorrect curvature, we carried out extensive Monte Carlo simulations. Approximately  $10^6$  proton events in the energy range of interest passed the BESS T0 trigger.

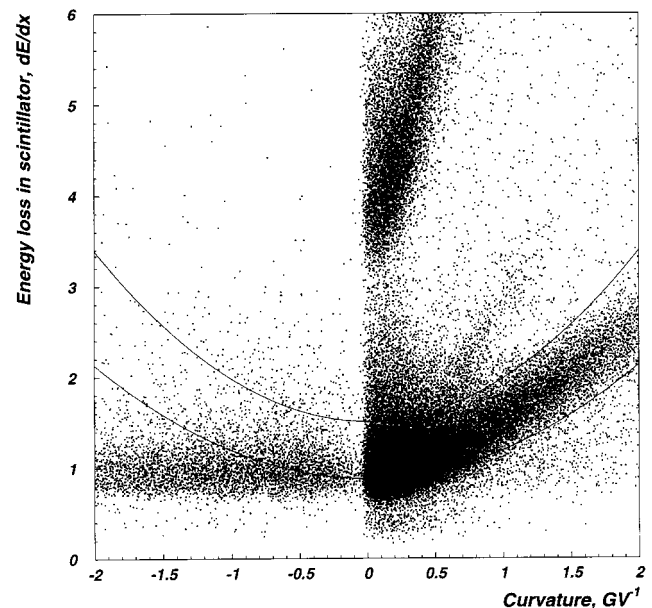


FIG. 4.—Ionization energy loss in scintillator ( $dE/dx$ ) vs. curvature with albedo removed. Lines correspond to the  $dE/dx$  selection criteria.

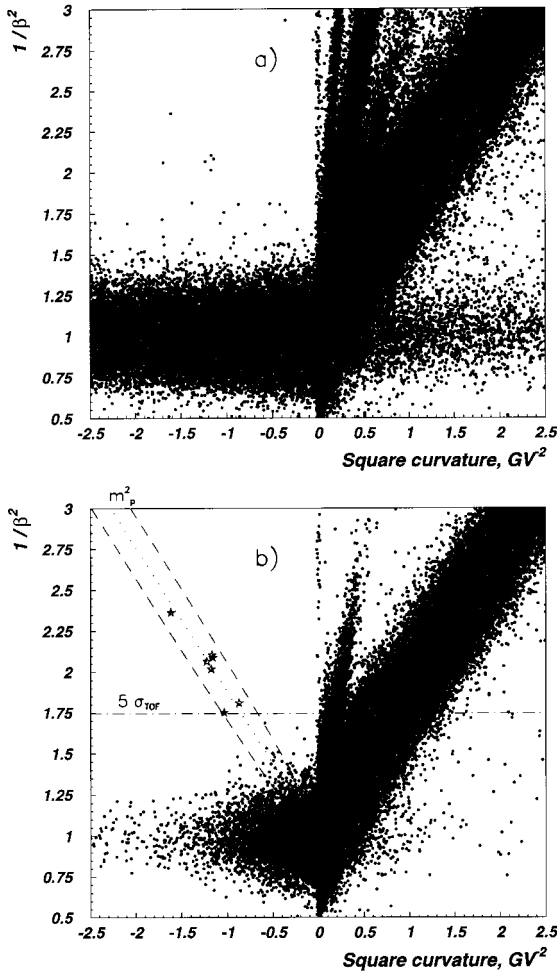


FIG. 5.—Inverse-square beta vs. square curvature with albedo removed: (a) before  $dE/dx$  selection; (b) after  $dE/dx$  selection. The seven antiproton events marked by stars are clearly seen lying along the straight dotted line corresponding to the proton mass. The dashed lines correspond to  $1\sigma_{m^2}$  deviation from the square proton mass.

In a simulation with  $10^7$  events, none produced negative curvature and none passed our selection criteria for antiprotons. Furthermore, we can split the JET chamber into two halves horizontally (in the  $y$ -direction), determine two curvatures for each event, and compare them. Within errors, all seven pairs agree with each other, and agree with the originally determined curvatures using the full chamber. We conclude that none of these events is due to a positively charged particle with a mismeasured curvature.

The most likely fake antiproton is a light particle with a large value of  $1/\beta$ . We can estimate the expected number of light relativistic negative particles that may pass the  $dE/dx$  selection and that have  $1/\beta$  larger than  $(1 + 5\sigma_{\text{TOF}})$ ,

TABLE 1  
BACKGROUND FROM LIGHT NEGATIVE PARTICLES

Rigidity (GV/c)	$N^-$ <sup>a</sup>	Number of Antiprotons	Expected Number of Fake Antiprotons
0.75–1.0.....	346	5	0.0001
1.0–1.25.....	1028	2	0.0003
1.25–1.5.....	1585	0	0.0005

<sup>a</sup> Number of negative events after  $dE/dx$  cuts.

assuming a Gaussian  $\beta^{-1}$  error distribution. This number is equal to  $2.9 \times 10^{-7} N^-$ , where  $N^-$  is a total number of negative light particles ( $e^-$ ,  $\mu^-$ ,  $\pi^-$ ) in a given energy bin;  $2.9 \times 10^{-7}$  corresponds to half the Gaussian probability for a  $5\sigma_{\text{TOF}}$  fluctuation. The estimation of background conditions due to this effect is presented in Table 1.

We have high confidence that these events are all antiprotons. All the events have measured square mass that deviates within  $1\sigma$  of the antiproton square mass. The  $\sigma$  comes from the uncertainties in  $\beta$  and  $R$ , and obtained from the flight data.

We determine the number of detected protons over the same energy range by using the same selection criteria. For this, we use the T0 low CD sample, applying the same  $dE/dx$  and  $5\sigma_{\text{TOF}}$  selections. The numbers of events in each step of data analysis are given in Table 2. The numbers obtained from the T0 low CD sample must be multiplied by the factor 140 in order to account for the sampling described earlier. The numbers are given in Table 3 in the column labeled  $N_{p,\text{obs}}$ , along with the efficiencies,  $\epsilon_{\text{cut}}$ , that account for the  $dE/dx$  and  $5\sigma_{\text{TOF}}$  selections. These same efficiencies applied to antiprotons.

#### 4.4. Determination of Fluxes

In order to obtain fluxes, we need to understand the instrumental and data analysis efficiencies, as well as the corrections for the overlying atmosphere. Some of efficiencies were calculated from flight data, and some from Monte Carlo simulations. To do these simulations, the GEANT-3.21 code was used. GEANT normally uses the GHEISHA code to do the simulation of the hadronic showers. We found that GHEISHA is not correct for the simulation of hadronic interactions of low-energy antiprotons (below about 1 GeV), and so, in place of its cross sections, we put the new experimental cross sections of the antiproton-nuclei inelastic hadronic interaction (Nakamura et al. 1984 and Kuzichev, Lepikhin, & Smirnitisky 1994) in the energy range 100–800 MeV and used this modified GEANT/GHEISHA code for simulation of the instrument response. With this improvement, the code reproduces experimental results and simulates more precisely the point of hadronic interaction, but it does not change the original

TABLE 2  
NUMBER OF EVENTS IN EACH STEP OF DATA ANALYSIS

Step	Total	T0 Low CD
Passed instrument.....	$\sim 10^8$	...
Recorded.....	3,635,139	517,148
Passed selections described in 4.2, all energies.....	1,580,030	72,144
Passed $dE/dx$ (proton band), all energies.....	752,658	47,286
Passed $dE/dx$ and $5\sigma_{\text{TOF}}$ , all energies.....	117,636	11,432
The same, but in the 200–600 MeV energy range.....	103,373	10,384 <sup>a</sup>
The same, but only negative curvatures ( $\bar{p}$ ).....	7	...

<sup>a</sup>  $10,384 \times 140$  is the total number of protons  $N_{p,\text{obs}}$  in Table 3.

TABLE 3  
SUMMARY OF OBSERVED NUMBERS AND EFFICIENCIES

ENERGY CORRECTED FOR TOA (MeV)	ANTIPROTON AND PROTON FACTORS		ANTIPROTON FACTORS AND NUMBERS				PROTON FACTORS AND NUMBERS		
	$\epsilon_{\text{det}}$	$\epsilon_{\text{cut}}$	$N_{\bar{p},\text{obs}}$	$\bar{\epsilon}_{\text{air}}$	$\epsilon_{\text{rig}}$	$\epsilon_{\text{annih}}$	$N_{p,\text{obs}}$	$\epsilon_{\text{air}}$	$k_{\text{air}}$
200–250 .....	0.26	0.96	0	0.85	1.0	0.74	203,420	0.95	0.78
250–300 .....	0.27	0.95	0	0.86	1.0	0.78	214,760	0.94	0.83
300–350 .....	0.29	0.95	1	0.87	0.99	0.81	231,420	0.94	0.91
350–400 .....	0.30	0.94	0	0.88	0.99	0.83	241,780	0.93	0.91
400–450 .....	0.31	0.88	4	0.88	0.99	0.85	209,020	0.93	0.92
450–500 .....	0.31	0.74	1	0.89	0.99	0.87	183,680	0.93	0.93
500–550 .....	0.31	0.46	1	0.89	0.98	0.88	108,220	0.94	0.93
550–600 .....	0.31	0.27	0	0.89	0.97	0.89	61,460	0.94	0.93
Error <sup>a</sup> .....	0.03	0.02	...	0.08	0.02	0.07	...	0.06	0.10

<sup>a</sup> These uncertainties apply to all the numbers in the column above.

GEANT/GHEISHA method for the simulation of secondary particle production. The probability of antiproton-nuclei inelastic hadronic interactions simulated by this modified code are about a factor of 2 lower than simulated by the original GHEISHA (see Appendix for more detail).

#### 4.4.1. Instrumental and Data Analysis Efficiencies

We need to know the efficiencies with which both protons and antiprotons passing through the active volume of the detector are registered. We combine all the off-line selections' efficiencies, described in § 4.2, in one value, assumed to be the same for both protons and antiprotons ( $\epsilon_{\text{det}}$ ), and give them in Table 3. These efficiencies include the hit-pattern selection efficiency applied on-line to the TT data and off-line to the CD sample. These efficiencies are obtained from raw data. A proton sample is selected using nonrestrictive  $dE/dx$  cuts in the scintillator pulse heights. Efficiencies are obtained from the number of events surviving after each selection. We assume that all proton events with hadronic interactions in the instrument were eliminated by one of the applied selections. It could be by the one track requirement selection, when an extra track (or tracks) was produced by a secondary particle, or by the total number of JET hits, or by the  $\chi^2$  selection that rejects cases of elastic scattering. Thus, the loss of protons due to hadronic interactions is accounted for in the  $\epsilon_{\text{det}}$ . We can apply the same  $\epsilon_{\text{det}}$  to antiprotons, but this will not account for antiproton annihilation reactions. We have to add one more factor,  $\epsilon_{\text{annih}}$ , to account for the additional reactions that remove antiprotons. This is most important at the low energies we are exploring here. To determine this factor, the passage of both protons and antiprotons through the instrument was simulated by the GEANT/GHEISHA Monte Carlo code modified according to the Appendix. The exact configuration of the BESS payload was put into GEANT with all real thicknesses and materials.<sup>12</sup> They are as follows:

*Pressurized vessel.*—0.5 g cm<sup>-2</sup> (Al).

*Gas.*—0.3 g cm<sup>-2</sup> (CO<sub>2</sub>).

*TOF.*—Two counters with 2.2 g cm<sup>-2</sup> each (94% scintillator, 6% Al).

*ODC.*—Two chambers with 0.76 g cm<sup>-2</sup> each (29% Al, 36% epoxy, 17% copper, 18% Mylar).

*Cryostat with magnet coil.*—Upper and lower part of cylinder with 4.5 g cm<sup>-2</sup> each (55% Al, 4% Mylar, 41% Nb/Ti/Al/Cu/Mylar conductor).

*IDC.*—Two chambers with 0.9 g cm<sup>-2</sup> each (30% Al, 31% epoxy, 15% copper, 24% Mylar).

*JET.*—0.13 g cm<sup>-2</sup> (20% epoxy, 25% copper, 55% Mylar).

The total thickness traversed by a normal incident particle to trigger the instrument is 17.8 g cm<sup>-2</sup>.

An isotropic beam incident on the instrument was simulated. The probabilities  $\epsilon_{\text{hadr}}$  of the particle passing through the instrument without hadronic interaction were calculated separately for protons and antiprotons according to the formula

$$\epsilon_{\text{hadr}}(E) = 1 - \left[ \frac{N_{\text{hadr}}(E) + N_{\text{sec}}(E)}{N_{\Sigma}(E)} \right],$$

where  $N_{\Sigma}$  is the total number of particles that passed through the instrument aperture,  $N_{\text{hadr}}$  is the number of events with inelastic hadronic interactions that occurred in the instrument above the bottom TOF (including this detector itself), and  $N_{\text{sec}}$  is the number of events in which a hadronic interaction occurred below the bottom TOF, and at least one upward-moving charged secondary passed through the TOF or any drift chamber.

All GEANT interactions were “ON” during simulations. The energy-dependent factor,  $\epsilon_{\text{annih}}$  in Table 3, is determined as a probability for an antiproton to pass through the instrument (from the top to bottom TOF counter) without hadronic interaction, with the condition that there is no secondary or other detected particle in the BESS detectors from an interaction below the bottom TOF counter, divided by the same probability for protons (as calculated above). It is assumed that all cases of elastic hadronic interaction are removed by the  $\chi^2$  cut.

Uncertainties in the cross sections used for modeling the low-energy hadronic interactions are included in the uncertainties in this factor. We see that BESS is sensitive to the low-energy antiprotons above 200 MeV. The sensitivity,  $\epsilon_{\text{annih}}$ , falls quickly at lower energies, where particles stop in the instrument itself.

Some events that undergo an inelastic hadronic interaction inside BESS will pass our cuts. To simulate this, we need to know precisely the kinematics and multiplicities of secondary particle production, their identity and spectra. The required double differential cross sections are not available for antiprotons in the energy range of our interest. To

<sup>12</sup> The code also includes all the structure, batteries, and other matter below and around the active detector described here. They are all located outside the projected field of view of the instrument.

simulate the production of secondaries, we used the original GEANT/GHEISHA; we must use these results with caution. Our assumption that all inelastic hadronic interactions are rejected means that we actually underestimate  $\epsilon_{\text{annih}}$  and overestimate the resulting antiproton flux. The exact result can be obtained only after calibrating BESS in an antiproton beam. This is included in a plan of our future activity.

Let us recall that antiprotons are taken from TT data where the rigidity selection was applied on board. We need to calculate the efficiency of this selection. To obtain it, we apply off-line the same selection to the CD data. The look-up table of the event deflection is identical to the table used in flight. These efficiencies are given in Table 3 in the column  $\epsilon_{\text{rig}}$ . The protons are taken directly from CD data, and so no rigidity selection correction is necessary.

#### 4.4.2. Correction for Overlying Atmosphere

We also correct the fluxes for the inelastic hadronic interactions in the atmosphere. We correct for ionization loss in the matter in and above the instrument, and we bin particles according to their energy at the top of atmosphere (TOA). The amount of residual atmosphere was taken to be  $5.0 \pm 0.2 \text{ g cm}^{-2}$ .

The probabilities of protons and antiprotons surviving after passing the residual atmosphere were calculated using the GEANT code. They are presented in Table 3 under the labels  $\epsilon_{\text{air}}$  and  $\bar{\epsilon}_{\text{air}}$ , respectively. All protons and antiprotons that undergo inelastic hadronic interactions in the simulated atmosphere are assumed to go undetected.

We also need to know the contribution to the proton and antiproton fluxes due to secondary production in the atmosphere. These calculations have been made by Papini, Grimani, & Stephens (1993) for protons and by Stephens (1993), Pfeifer, Roster, & Simon (1996), and Mitsui (1996) for antiprotons. The primary proton flux used in the two latter papers is very similar, and the derived secondary antiproton fluxes are in a good agreement. The correction factor for secondary proton production,  $k_{\text{air}}$ , was retrieved from Papini et al. (1993) and adjusted for the solar modulation for the flight date. The  $k_{\text{air}}(E)$  we used are shown in Table 3.

The expected number of atmospheric antiprotons  $N_{\bar{p},\text{atm}}$  incident on BESS was estimated according to Pfeifer et al. (1996) to be  $7.0 \pm 2.5$  antiprotons in the energy range from 200 to 600 MeV. Note that only about 20% of these would be detected because of overall detection efficiency.

#### 4.4.3. The Antiproton Flux and Antiproton/Proton Ratio

Now we know all of the efficiencies and correction factors in order to determine the antiproton flux and the antiproton/proton ratio. Combining all efficiencies and corrections from Table 3, as well as corrections for the antiproton production in the atmosphere,  $N_{\bar{p},\text{atm}}$ , we calculate the numbers of protons  $N_p^{\text{TOA}}(E)$  and antiprotons  $N_{\bar{p}}^{\text{TOA}}(E)$  at the TOA according to the formulas

$$N_p^{\text{TOA}}(E) = \frac{k_{\text{air}}(E)N_{p,\text{obs}}(E)}{\epsilon_{\text{air}}(E)\epsilon_{\text{det}}(E)\epsilon_{\text{cut}}(E)},$$

$$N_{\bar{p}}^{\text{TOA}}(E) = \frac{1}{\bar{\epsilon}_{\text{air}}(E)} \left[ \frac{N_{\bar{p},\text{obs}}(E)}{\epsilon_{\text{rig}}(E)\epsilon_{\text{det}}(E)\epsilon_{\text{annih}}(E)\epsilon_{\text{cut}}(E)} - N_{\bar{p},\text{atm}}(E) \right].$$

We have combined all energy bins to improve the antiproton statistics. We realize that by doing this we increase the uncertainty due to possible energy dependence of the antiproton flux in this energy range. The antiproton flux is given by

$$F_{\bar{p}}(200\text{--}600 \text{ MeV}) = \frac{1}{T_{\text{live}} G \Delta E} \sum_{\text{all } E} N_{\bar{p}}^{\text{TOA}}(E),$$

where  $T_{\text{live}}$  is the live time,  $G$  is the geometrical factor,  $\Delta E$  is our energy range corrected to the TOA. The flux is  $6.4^{+5.5}_{-3.5} \times 10^{-3} (\text{m}^2 \text{ sr s GeV})^{-1}$ .

The antiproton/proton ratio is calculated from

$$R_{\bar{p}/p}(200\text{--}600 \text{ MeV}) = \frac{\sum_{\text{all } E} N_{\bar{p}}^{\text{TOA}}(E)}{\sum_{\text{all } E} N_p^{\text{TOA}}(E)},$$

and has a value of  $5.2^{+4.4}_{-2.8} \times 10^{-6}$ .

The detailed Monte Carlo studies mentioned above show that, even though BESS has about  $20 \text{ g cm}^{-2}$  of material in the active part of the detector,  $K^-$  mesons produced by interactions are rejected efficiently by the multiple-particle tracking capability. We estimate that the ratio of the locally produced  $K^-$  mesons to the protons for the BESS energy range is  $(2\text{--}3) \times 10^{-7}$ , so this background is certainly negligible.

## 5. DISCUSSION

We believe we have carried out a very difficult task, namely, that of finding a measurable signal of antiprotons in a “background” of positively charged particles  $10^6$  times as abundant, and of lighter negatively charged particles  $10^4$  times as abundant. Our result is consistent with current calculations without assuming any exotic source. Figure 6 shows our antiproton flux, along with the recent results in

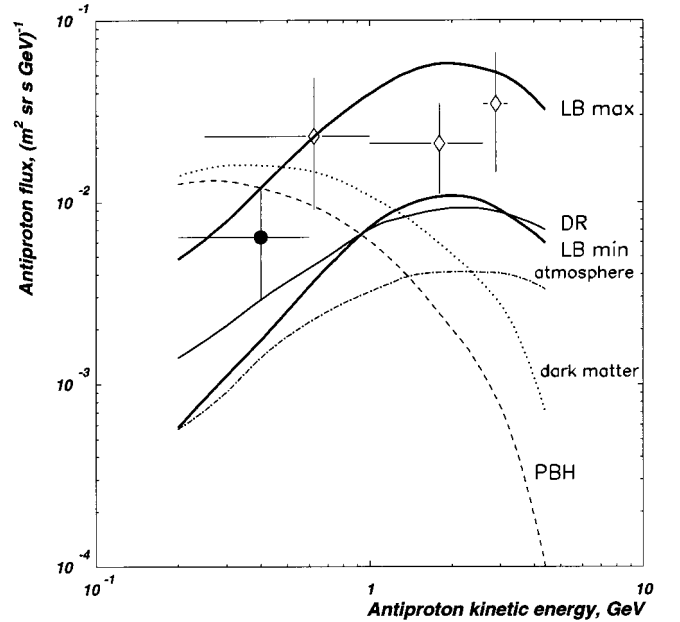


FIG. 6.—Antiproton flux obtained in this work (filled circle) and by IMAX (open diamonds). The maximum and minimum antiproton spectra as calculated by Gaisser & Shaeffer (1992) according to the Leaky Box model (LB, thick solid line) and as calculated by Mitsui (1996) according to DR model (DR, solid line). The dot-dashed line is the atmospheric antiproton background as calculated by Pfeifer et al. (1996). Dotted line: shape of antiproton spectrum produced due to dark matter particles annihilation according to Bottino et al. (1995); dashed line: shape of spectrum produced due to PBH evaporation as given by Maki et al. (1996). All calculated spectra are modulated for the BESS-93 flight date.

the low-energy region obtained by the IMAX group (Mitchell et al. 1996). We show both results in one plot, without any correction for different solar modulation; the estimated difference in the antiproton flux due to modulation is less than 10%. Both of these measurements are consistent with the range of antiproton flux allowed by the calculation of Gaisser & Shaeffer (1992) and modulated for the BESS-93 flight date. The range is partially due to the difference in the assumed proton flux. The proton flux obtained in this experiment (Seo et al. 1995) is closer to the proton flux that gave the minimum antiproton flux in these calculations. These calculations were done assuming a simple Leaky Box (LB) model of galactic cosmic-ray propagation (an equilibrium model with sources evenly distributed in space). All cosmic rays are assumed to wander throughout our Galaxy, scattering off the magnetic irregularities and undergoing interactions with interstellar matter. There is some probability of their leaving the system (of order 1/1000) on an encounter with the border. In this model, antiprotons are secondary and produced in the cosmic ray–interstellar matter nuclear interactions. Mitsui (1996) calculated the expected flux in the three-dimensional diffusive reacceleration (DR) model (Heinbach & Simon 1995), which includes the effects of additional acceleration (or reacceleration) in encounters with turbulent magnetic fields in the interstellar medium. For his calculations, Mitsui (1996) used the proton flux from Seo et al. (1991), which is approximately the same as the proton flux measured in this experiment (Seo et al. 1995). The results he obtained are consistent with our measured antiproton flux. To use antiproton measurements in order to determine whether the LB model can be differentiated from a more sophisticated DR model will require measurements with much better statistical precision (of order 5% for lower than 500 MeV antiprotons).

There is a significant difference with the results of Buffington et al. (1981) for the 130–320 MeV energy range. Our lowest energy-detected antiproton has an energy of 330 MeV, and we obtain an antiproton/proton ratio upper limit from our data in the energy range of overlap with Buffington et al. (1981) (200–300 MeV) as  $1.3 \times 10^{-5}$  (95% confidence level).

Antiprotons could also be produced in some exotic processes such as by the evaporation of primordial black holes (PBH) or by the annihilation or decay of dark matter—for example, a supersymmetric particle like neutralino. These processes produce an almost energy-independent antiproton-to-proton ratio down to very low energy; con-

ceivably, the flux of antiprotons from these processes may dominate below 500 MeV. The ranges of expected modulated contributions from these models to the antiproton flux (taken from Maki et al. 1996 for PBH and from Bottino et al. 1995 for dark matter) are shown in Figure 6. One can see that the puzzle of the low-energy antiproton origin is still not solved, and a precise measurement of the shape of the antiproton spectrum in the low-energy region is needed to help solve it.

In the assumption that all the antiproton flux with energy less than 300 MeV is produced by PBH evaporation within 3–5 kpc, Maki et al. (1996) estimate the upper limit for the rate of PBH evaporation in the solar vicinity to be  $1.7 \times 10^{-2} \text{ pc}^{-3} \text{ yr}^{-1}$ . Also, we show here for comparison the flux of secondary antiprotons produced in  $5 \text{ g cm}^{-2}$  of air as given by Pfeifer et al. (1996). Their calculation was based on a flux of protons essentially the same as that measured in this experiment (Seo et al. 1995). We used these results for our secondary antiproton correction.

This experiment has detected antiprotons below 600 MeV and has made the first high-sensitivity peek into a window where evidence for exotic antimatter sources might be found. Subsequent BESS flights will make use of analysis techniques described here, in order to obtain much higher statistics measurements. At least 4 times as many antiprotons have already been found, and we hope to double that number again with a flight in the summer of 1996. Charge-sign dependence of solar modulation will be studied with flights over several years at solar minimum and beyond.

The authors would like to thank W. V. Jones of NASA/GSFC Headquarters, Professor A. Nishida, Director General of ISAS, Professor H. Sugawara, Director General of KEK, and Professor S. Iwata of KEK for their support and encouragement. The authors would also like to express their sincere appreciation to the NASA/GSFC/WFF Balloon office and the NSBF for their skillful handling of the ballooning expedition, and the launch and recovery of the payload. We appreciate the valuable help of D. Righter in the realization of the launch, and J. Krizmanic in the installation of the BESS software at GSFC. We also thank A. Buffington for his careful review and critique of our manuscript, and Heather Muise for help in finding a way to replace the cross sections in GHEISHA. This work is supported by Grant-in-Aid for Scientific Research in Monbusho, Japan.

## APPENDIX

### CALCULATION OF HADRONS INTERACTION PROBABILITY WITH NEW EXPERIMENTAL CROSS SECTIONS

Following the definitions in the GHEISHA manual (Fesefeldt 1985), we identify the elastic hadronic interaction only with the coherent elastic interaction. We combine the coherent inelastic, incoherent elastic, and incoherent inelastic in the total inelastic (absorption) hadronic interaction, which includes the annihilation process. The total inelastic cross sections for antiprotons were measured by Nakamura et al. (1984) and by Kuzichev et al. (1994). Kuzichev et al. (1994) claimed the measurement of the annihilation cross section, but, following the definition given above, they have measured the total inelastic cross section. Nakamura et al. (1984) made the measurements for C, Al, and Cu targets and six values of antiproton momentum from 466 to 879 MeV/c. Kuzichev et al. (1994) measured cross sections for Be, C, Al, Fe, Cu, Cd and, Pb targets and for six values of momentum from 700 to 2500 MeV/c. The results obtained by these two groups agree very well. Understanding that GEANT/GHEISHA does not provide the correct results for the attenuation of low-energy antiprotons,

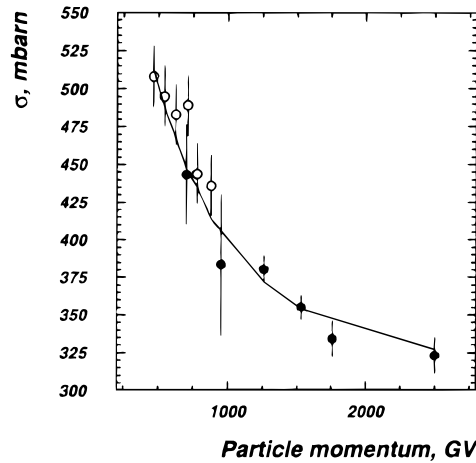


FIG. 7a

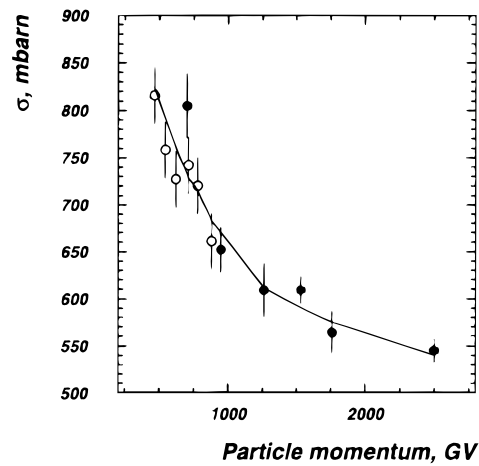


FIG. 7b

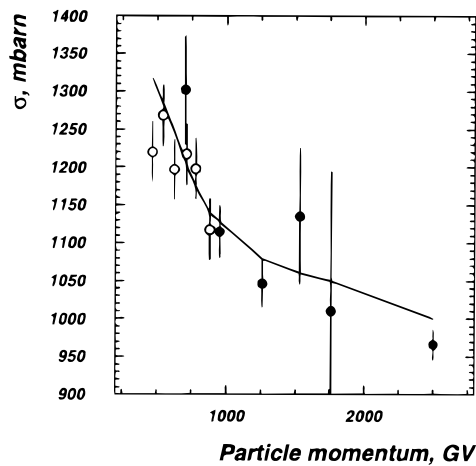


FIG. 7c

FIG. 7.—Inelastic hadronic cross sections for antiprotons for different targets: (a) for  $C_6^{12}$ , (b) for  $Al_{13}^{27}$ , and (c) for  $Cu_{29}^{64}$ . Solid line: calculated with fitted  $a_0$ ,  $a_1$ , and  $a_2$ ; open and filled circles: experimental values taken from Nakamura et al. (1984) and from Kuzichev et al. (1994), respectively.

we used the Nakamura et al. (1984) and Kuzichev et al. (1994) experimental cross sections to calculate the correction for the antiproton attenuation in the atmosphere and in the detector.

To extend the experimental cross sections for any nuclei, we used the approximation

$$\sigma_{\bar{p},A} = A^{2/3}(a_0 + a_1 Z + a_2 Z^2)$$

taken from Kuzichev et al. (1994). The parameters  $a_0(P)$ ,  $a_1(P)$ , and  $a_2(P)$  depend on the antiproton momentum,  $P$ , in the manner tabulated by Kuzichev et al. (1994) and fitted by us for the continuous values of  $P$ . Using this formula, we recalculated and replaced the GHEISHA's variable SHADR (distance to the next point of interaction). By doing this, we could use the powerful GEANT/GHEISHA code for tracking and simulating interactions with the correct values of the cross sections.<sup>13</sup> Figures 7a–7c show the cross sections for C, Al, and Cu that we calculated by this technique and that we used for our simulations, along with experimental values from Nakamura et al. (1984) and Kuzichev et al. (1994). To check the proper modification, we simulated, by a modified GEANT/GHEISHA, the probability of inelastic hadronic interaction of antiprotons in a 2 cm thick sample of Al, turning off the energy-loss process. The results are compared in Figure 8 with attenuation  $p(\Delta)$  calculated according to

$$p(\Delta) = 1 - \exp(-\Delta/\lambda_0).$$

The attenuation length is given by

$$\lambda_0 = \frac{A10^4}{6.022\rho\sigma(\text{mbarn})} (\text{cm}),$$

where  $A$  and  $\rho$  are the target atomic weight and density, respectively, and  $\sigma$  was taken according to Figure 7b. The filled circles in Figure 8 correspond to the results of simulation by our modified GEANT/GHEISHA code and show a good agreement with curve. The open circles show the same probabilities obtained by the original GEANT/GHEISHA.

<sup>13</sup> Actually, we noticed that GHEISHA carries inelastic cross sections for antiprotons that differ not too much from those used by us (for higher than 200 MeV). However, we found a “bug” that effectively doubles the interaction probability for antiprotons.

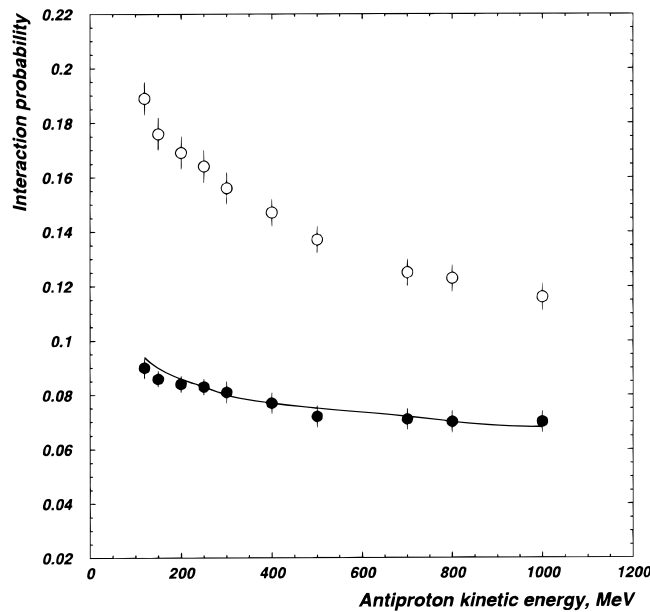


FIG. 8.—Probability of the inelastic hadronic interaction of antiprotons in 2 cm of Al. *Solid line*: as calculated with new cross sections (Fig. 7b, *solid line*); *filled circles*: as simulated by GEANT with these new cross sections installed; *open circles*: as simulated by GEANT/GHEISHA with the original cross sections.

To revise the GEANT/GHEISHA simulation for protons, we replaced the proton inelastic cross sections with the approximation reported in Silberberg & Tsao (1990):

$$\sigma_{p,A}^{\text{inel}} = \sigma_{h,e}^{\text{inel}} [1 - 0.62 \exp(-E/200) \sin(10.9E^{-0.28})],$$

where  $\sigma_{h,e}^{\text{inel}} = 45A^{0.7} [1 + 0.016 \sin(5.3 - 2.63 \ln A)]$  mbarn is the total inelastic cross section measured at high energy,  $A$  is the target atomic weight, and  $E$  is the energy in MeV. This approximation is applicable over the whole range of elements from lithium to uranium. Silberberg & Tsao (1990) claim their approximation fits the experimental data with 2% precision above 300 MeV and about 5% between 100 and 300 MeV. For the lighter nuclei, we used the original GHEISHA cross sections. We also checked the proper replacement and noticed some difference with the original code, but not so significant as in the case of antiprotons.

#### REFERENCES

- Ahlen, S. P., et al. 1988, *Phys. Rev. Lett.*, 61, 145  
 Anraku, K., et al. 1994, *Adv. Space Res.*, 17, 101  
 Bogomolov, E. A., et al. 1979, 16th Int. Cosmic Ray Conf. (Kyoto), 1, 330  
 Bottino, A., et al. 1995, *Nucl. Phys. B (Proc. Suppl.)*, 43  
 Buffington, A., Schindler, S. M., & Pennypacker, C. R. 1981, *ApJ*, 248, 1179  
 Fesefeldt, H. 1985, GHEISHA, The Simulation of Hadronic Showers (Geneva: CERN)  
 Gaisser, T. K. 1990, *Cosmic Rays and Particle Physics* (Cambridge: Cambridge Univ. Press)  
 Gaisser, T. K., & Shaeffer, R. K. 1992, *ApJ*, 394, 174  
 Gleeson, L. J., & Axford, W. I. 1968, *ApJ*, 154, 1011  
 Golden, R. L., et al. 1979, *Phys. Rev. Lett.*, 43, 1196  
 ———. 1991, *Nucl. Instrum. Methods Phys. Res.*, 306(A), 366  
 Heinbach, U., & Simon, M. 1995, *ApJ*, 441, 209  
 Jungman, G., & Kamionkowski, M. 1994, *Phys. Rev. D*, 49, 5  
 Kiraly, P., Wdowczyk, J., & Wolfendale, A. 1981, *Nature*, 293, 120  
 Kuzichev, V., Lepikhin, Yu., & Smirnitky, V. 1994, *Nucl. Phys. A*, 576, 581  
 Maki, K., Mitsui, T., & Orito, S. 1996, *Phys. Rev. Lett.*, 76, 344  
 Makida, Y., et al. 1992, *Adv. Cryog. Eng.*, 37(A), 401  
 Mitchell, J., et al. 1993, 23d Int. Cosmic Ray Conf. (Calgary), 1, 519  
 ———. 1996, *Phys. Rev. Lett.*, 76, 3057  
 Mitsui, T. 1996, Ph.D. thesis, Univ. Tokyo  
 Nakamura, K., et al. 1984, *Phys. Rev. Lett.*, 52, 731  
 Papini, P., Grimani, C., & Stephens, S. A. 1993, 23d Int. Cosmic Ray Conf. (Calgary), 3, 761  
 Pfeifer, C., Roster, S., & Simon, M. 1996, *Phys. Rev. C*, 54, 882  
 Rudaz, S., & Stecker, F. 1988, *ApJ*, 325, 16  
 Salamon, M. H., et al. 1990, *ApJ*, 349, 78  
 Seo, E. S., et al. 1991, *ApJ*, 378, 763  
 ———. 1995, 24th Int. Cosmic Ray Conf. (Rome), 2, 648  
 ———. 1996, in preparation  
 Silberberg, R., & Tsao, C. H. 1990, *Phys. Rep.*, 191, 351  
 Silk, J., & Srednicki, M. 1984, *Phys. Rev. Lett.*, 53, 624  
 Simon, M., & Heinbach, U. 1996, *ApJ*, 456, 519  
 Steigman, G. 1976, *ARA&A*, 14, 339  
 Stephens, S. A. 1993, 23d Int. Cosmic Ray Conf. (Calgary), 2, 144  
 Stephens, S. A., & Golden, R. L. 1987, *Space Sci. Rev.*, 46, 31  
 Stochaj, S. J., et al. 1990, 21st Int. Cosmic Ray Conf. (Adelaide), 3, 284  
 Streitmatter, R. E., et al. 1989, *Adv. Space Res.*, 9, 1265  
 Tomasch, A. D., et al. 1995, 24th Int. Cosmic Ray Conf. (Rome), 3, 599  
 Turner, M. 1982, *Nature*, 297, 379  
 Webber, W., & Potgieter, M. 1989, *ApJ*, 344, 779  
 Yamamoto, A., et al. 1988, *IEEE Trans. MAG*, 24(2), 1421  
 ———. 1994, *Adv. Space Res.*, 14, 75  
 Yoshimura, K., et al. 1995, *Phys. Rev. Lett.*, 75, 3792